

DYNAMIC GLUCOSE ENHANCED IMAGING USING DIRECT WATER SATURATION

LINDA KNUTSSON^{1,2,3}, NIRBHAY N. YADAV^{1,4}, SAJAD MOHAMMED ALI³, DAVID OLAYINKA KAMSON^{2,5},
ELENI DEMETRIOU^{1,4}, ANINA SEIDEMO⁶, LINDSAY BLAIR², DORIS D. LIN⁴, JOHN LATERRA^{2,5,7,8}, AND
PETER C. M. VAN ZIJL^{1,4,9}

¹*F.M. KIRBY RESEARCH CENTER FOR FUNCTIONAL BRAIN IMAGING, KENNEDY KRIEGER INSTITUTE, BALTIMORE, MD, US*

²*DEPARTMENT OF NEUROLOGY, JOHNS HOPKINS UNIVERSITY SCHOOL OF MEDICINE, BALTIMORE, MD, US*

³*DEPARTMENT OF MEDICAL RADIATION PHYSICS, LUND UNIVERSITY, LUND, SWEDEN*

⁴*RUSSELL H. MORGAN DEPARTMENT OF RADIOLOGY AND RADIOLOGICAL SCIENCE,
JOHNS HOPKINS UNIVERSITY SCHOOL OF MEDICINE, BALTIMORE, MD, US*

⁵*DEPARTMENT OF ONCOLOGY, JOHNS HOPKINS UNIVERSITY SCHOOL OF MEDICINE, BALTIMORE, MD, US*

⁶*DIAGNOSTIC RADIOLOGY, DEPARTMENT OF CLINICAL SCIENCES, LUND UNIVERSITY, LUND, SWEDEN*

⁷*HUGO W. MOSER RESEARCH INSTITUTE AT KENNEDY KRIEGER, BALTIMORE, MD, US*

⁸*DEPARTMENT OF NEUROSCIENCE, JOHNS HOPKINS UNIVERSITY SCHOOL OF MEDICINE, BALTIMORE, MD, US*

⁹*DEPARTMENT OF BIOMEDICAL ENGINEERING, JOHNS HOPKINS UNIVERSITY SCHOOL OF MEDICINE, BALTIMORE, MD, US*

ABSTRACT

Purpose: Dynamic glucose enhanced (DGE) MRI studies employ chemical exchange saturation transfer (CEST) or spin lock (CESL) to study glucose uptake. Currently, these methods are hampered by low effect size and sensitivity to motion. To overcome this, we propose to utilize exchange-based linewidth (LW) broadening of the direct water saturation (DS) curve of the water saturation spectrum (Z-spectrum) during and after glucose infusion (DS-DGE MRI).

Methods: To estimate the glucose-infusion-induced LW changes (ΔLW), Bloch-McConnell simulations were performed for normoglycemia and hyperglycemia in blood, gray matter (GM), white matter (WM), CSF, and malignant tumor tissue. Whole-brain DS-DGE imaging was implemented at 3 tesla using dynamic Z-spectral acquisitions (1.2 s per offset frequency, 38 s per spectrum) and assessed on four brain tumor patients using infusion of 35 g of D-glucose. To assess ΔLW , a deep learning-based Lorentzian fitting approach was employed on voxel-based DS spectra acquired before, during, and post-infusion. Area-under-the-curve (AUC) images, obtained from the dynamic ΔLW time curves, were compared qualitatively to perfusion-weighted imaging (PWI).

Results: In simulations, ΔLW was 1.3%, 0.30%, 0.29/0.34%, 7.5%, and 13% in arterial blood, venous blood, GM/WM, malignant tumor tissue, and CSF, respectively. *In vivo*, ΔLW was approximately 1% in GM/WM, 5-20% for different tumor types, and 40% in CSF. The resulting DS-DGE AUC maps clearly outlined lesion areas.

Conclusions: DS-DGE MRI is highly promising for assessing D-glucose uptake. Initial results in brain tumor patients show high-quality AUC maps of glucose-induced line broadening and DGE-based lesion enhancement similar and/or complementary to PWI.

KEYWORDS: DYNAMIC GLUCOSE ENHANCED (DGE) MRI, CEST, Z-SPECTRA, DIRECT SATURATION (DS), GLUCOCEST

CORRESPONDING AUTHOR: LINDA KNUTSSON, EMAIL: LKNUTSS1@JHU.EDU

1 Introduction

Contrast agents play a major role in MRI for both research and clinical routine. The most common ones, Gadolinium (Gd) based, are well established but may cause side effects such as nephrogenic systemic fibrosis [1, 2], limiting their use in certain patient groups, and *in vivo* deposition in tissues [3-5], leading to the FDA issuing a Box Package Warning on Gd contrast agents which remain under continued review [6]. In addition, many malignant tumors show little to no Gd-enhancement [7, 8]. Consequently, the current clinical practice is judicious use of Gd-based contrast agents, particularly in the young and vulnerable populations [9]. Thus, there is a need and interest in developing new contrast agents. The availability of chemical exchange saturation transfer (CEST) [10-17] and chemical exchange sensitive spin lock (CESL) [18-29] approaches has opened the MRI field to non-metallic contrast agents. CEST exploits the transfer of RF saturation from solute protons to water protons, leading to water signal loss, allowing detection of millimolar concentration solutes with MRI. CESL exploits signal dephasing due to exchange by applying a spin lock pulse with frequency (γB_1) set to match the exchange rate between solute and water protons, allowing measurement of the longitudinal relaxation time in the rotating frame ($T_{1\rho}$). When D-glucose (D-Glc) is used as an agent, these approaches have been dubbed glucoCEST and glucoCESL, respectively.

Dynamic glucose enhanced (DGE) MRI applies CEST or CESL of sugars dynamically, providing information on contrast agent uptake in tissues in a manner similar to dynamic contrast-enhanced (DCE) and dynamic susceptibility contrast (DSC) MRI [13, 14, 23-25, 27, 28, 30-35]. Unfortunately, the DGE MRI signal changes at clinical field strengths (3 T) have been on the order of one percent [17, 32], making the method sensitive to motion artifacts, especially when based on a single signal intensity from one saturation offset frequency per dynamic [36, 37]. Here, we propose to reduce these problems by utilizing the transverse relaxation effect originating from the hydroxyl proton groups having a chemical shift difference with the water proton pool. The exchange between these proton pools in glucose and water leads to spins experiencing different precession frequencies before and after exchange [38, 39]. This results in a collective phase dispersion, which yields a linewidth (LW) broadening of the direct saturation (DS) line shape in water saturation spectra (Z-spectra). We exploit this exchange-based relaxation enhancement to assess changes in D-Glc concentration by acquiring DS spectra using RF saturation of short duration and low B_1 . This approach is used commonly in CEST MRI in the Water Saturation Shift Referencing (WASSR) method [40] for measuring B_0 shifts, since it minimizes the contributions from saturation transfer (ST) effects from sources such as semi-solid magnetization transfer contrast (MTC), CEST, and relayed nuclear Overhauser effects (NOEs) [41]. This allows fitting of the full DS spectrum to a Lorentzian [42], a method recently optimized using a deep learning (DL) approach [43].

This study, therefore, aimed to develop a WASSR-analogous DGE method to utilize glucose-induced increases in the DS linewidth, dubbed DS-DGE MRI. The feasibility of the method at 3 T was investigated through simulations and for D-Glc infusions in brain tumor patients. Qualitative comparisons were made with DCE- and DSC-MRI.

2 Methods

2.1 Simulations

Bloch-McConnell simulations of Z-spectra at 3 T before and after D-Glc infusion were performed using Pulseseq-CEST [44]. Five tissues were simulated: blood (b), gray matter (GM), white matter (WM), malignant tumor with blood-brain barrier (BBB) disruption (TUMOR), and CSF. Importantly, hydroxyl exchange properties and water transverse relaxation times may differ between tissue compartments, leading to different signal contributions. Therefore, following a recently established model [45], three tissue compartments were simulated within WM, GM and TUMOR, namely blood (b), extravascular extracellular space (EES), and cell (c). Furthermore, within blood, we assumed arteriolar (a) and venular (v) compartments. We simulated a change in blood D-Glc concentration from a normoglycemic (baseline) level of 6.15 mM (111 mg/dL) to a hyperglycemic level of 19.8 mM (356 mg/dL) [45, 46]. The resulting compartmental D-Glc concentrations after transport ([45], Table 1) were used to calculate the Z-spectral intensities, $\frac{S(\Delta\omega)}{S_0}$, at 0.66, 1.28, 2.08, and 2.88 ppm, the offset frequencies ($\Delta\omega$) of the four hydroxyl proton pools described by Zaiss et al. [47]. All compartments, except for TUMOR EES, were assumed to have a pH of 7.2, with hydroxyl proton exchange rates of 2900, 6500, 5200 and 14300 Hz, respectively, at 37°C [47]. For TUMOR EES, a pH of 6.8 was assumed, leading to exchange rates of 1500, 3100, 2500 and 6000 Hz [47], respectively. Compartmental Z-spectra were simulated using 41 frequency offsets: $\pm 10, \pm 5.0, \pm 4.0, \pm 3.0, \pm 2.5, \pm 2.0, \pm 1.75, \pm 1.5, \pm 1.25, \pm 1.0, \pm 0.80, \pm 0.65, \pm 0.55, \pm 0.48, \pm 0.40, \pm 0.33, \pm 0.26, \pm 0.18, \pm 0.11, \pm 0.036, 0.0$ ppm. Saturation was applied using a train of ten 50-ms sinc-gaussian pulses, resulting in a total saturation time (t_{sat}) of 0.5 s. The simulations were performed using a $B_{1\text{peak}}$ of 0.5 μT .

The Z-spectra in GM, WM, and TUMOR were calculated by adding the normalized signal of three tissue compartments: blood (b), EES (e), and cell (c) [45]:

$$\frac{S_{tis}(\Delta\omega)}{S_0} = \left[f_{b,tis}\rho_b^{V/V} \left\{ f_a \frac{S_a(\Delta\omega)}{S_{0a}} + f_v \frac{S_v(\Delta\omega)}{S_{0v}} \right\} + f_{e,tis}\rho_e^{V/V} \frac{S_{e,tis}(\Delta\omega)}{S_{0e}} + f_{c,tis}\rho_{c,tis}^{V/V} \frac{S_{c,tis}(\Delta\omega)}{S_{0c}} \right] / \rho_{tis}^{V/V}, \quad (1)$$

with $f_{i,tis}$ being the volume fractions for compartment i (mL compartment/mL tissue) (Table 1). Blood in the capillaries was assumed to have fast deoxygenation, resulting in the blood compartment (b) consisting of only arteriolar (a) and venular (v) subcompartments [48] with volume fractions $f_a = 0.3$ and $f_v = 0.7$ in mL/mL blood, respectively. Since MR contrast is determined by water-based compartmental concentrations and tissue volume fractions, corrections are included for $\rho^{V/V}$, the water content per mL compartment or tissue (Table 1). After adding the Z-spectra from each compartment, Rician noise was added with a noise level of 2%, and the resulting tissue Z-spectra were re-sampled at frequencies used in the experiments (28 frequencies from -5 to 5 ppm), followed by fitting using a deep-learning Lorentzian fitting approach [43]. Thereafter, the difference in linewidth (ΔLW) between normoglycemia (baseline) and hyperglycemia was calculated for each tissue using Eq. 2 below.

Table 1: Relaxation times*, fractional volumes, D-Glc concentrations, and water contents for tissues (b, GM, WM, TUMOR, CSF) and their compartments (arterial, venous, EES, cell).

PARAMETER	TISSUE					
	Arterial Blood	Venous Blood	GM	WM	TUMOR	CSF
$T_{1,b}$ (s)	1.91	1.73				
$T_{1,tis}^e$ (s)			3.48	3.48	3.48	3.48
$T_{1,tis}^c$ (s)			1.08	0.65	1.02	
$T_{2,b}$ (s)	0.152	0.052				
$T_{2,tis}^e$ (s)			2.78	2.78	2.78	2.78
$T_{2,tis}^c$ (s)			0.071	0.055	0.071	
$f_{comp,b}$ (mL comp/mL b)	0.30	0.70				
$f_{b,tis}$ (mL b/mL tis)			0.038	0.018	0.050	0.00
$f_{e,tis}$ (mL EES/mL tis)			0.22	0.22	0.50	1.00
$f_{c,tis}$ (mL cell/mL tis)			0.74	0.76	0.45	0.00
C_b ngl (mM)	6.15	5.47				
$C_{e,tis}$ ngl (mM)			2.24	2.42	5.45	3.69
$C_{c,tis}$ ngl (mM)			0.167	0.381	0.811	
C_b hgl (mM)	19.8	19.1				
$C_{e,tis}$ hgl (mM)			6.10	5.71	17.6	11.9
$C_{c,tis}$ hgl (mM)			1.16	1.24	4.41	
$\rho_b^{V/V}$ (mL water/mL b)			0.856	0.856	0.856	
$\rho_e^{V/V}$ (mL water/mL comp)			0.938	0.938	0.938	
$\rho_c^{V/V}$ (mL water/mL comp)			0.809	0.678	0.674	
$\rho_{tis}^{V/V}$ (mL water/mL tis)			0.839	0.738	0.815	

*OH was set to have a T_1 of 1.20 s and T_2 of 0.100 s. ** For arterial and venous blood, a well-mixed compartment (fast exchange for water between plasma and erythrocytes) was assumed for the 500 ms saturation period. Relaxation times were calculated based on [62, 63], using: <https://www.kennedykrieger.org/physiologic-metabolic-anatomic-biomarkers/resources/software-and-databases/blood-t2-t1-hct-and-oxygenation-calculator> and the following settings: 3 T; t_{cp} 50 ms; t_p 50 ms; Hematocrit (Hct) 0.4; Oxygenations (Y) 0.98 and 0.60 for arterial and venous blood, respectively. Abbreviations: f , volume fraction ($f_a+f_v=1$, $f_{b,tis}+f_{e,tis}+f_{c,tis}=1$); C , D-Glc concentration; $\rho^{V/V}$, water volume density; $comp$, compartment; tis , tissue; a , arterial; v , venous; b , blood; e , EES; c , Cell; ngl , normoglycemia; hgl , hyperglycemia. Values for f , C , and $\rho^{V/V}$ are from ref. [45] and references therein.

2.2 Experiments

2.2.1 Patients

Four patients diagnosed with brain tumors were studied (one with an IDH-wildtype glioblastoma, two with a grade 2 IDH-mutated astrocytoma, and one with ALK-mutated non-small-cell lung cancer metastases). Written informed consent was obtained from each participant, and the project was approved by the local Institutional Review Board (IRB). Participants were asked to fast six hours before the study, but clear liquids were permitted. Before the start of the MRI examination, blood was drawn to verify that the baseline glucose levels were in the normal range (3.9–7.0 mM).

2.2.2 MRI Acquisition Protocol

Patients were examined on a 3 T Philips Elition RX system (Philips Healthcare, Best, the Netherlands). Pre- and post-contrast enhanced T_1 -MPRAGE, FLAIR, DS-DGE, DCE and DSC images were acquired during the same session. Conventional MR sequence parameters were: 1) T_1 -MPRAGE: TR/TE/FA=7.5 ms/3.5 ms/8°, FOV=212×212 mm², resolution=1.1×1.1×2.2 mm³, inversion time=755 ms, acquisition time=1 min 46 s, and 2) FLAIR: TR/TE= 11,000/120 ms, FOV=212×212 mm², resolution=1.1×1.1×2.2 mm³, inversion time=2800 ms, acquisition time=3 min 51 s.

DS-DGE images were acquired using a train of ten 50-ms sinc-gaussian pulses of $B_{1\text{peak}}$ of 0.5 μT and $t_{\text{sat}}=0.5$ s, followed by a whole-brain simultaneous multi-slice readout (multi-band factor 3). A total of 27 slices with FOV of 208×208 mm² and a resolution of 2.2×2.2×4.4 mm³ were acquired using TE/FA=17 ms/52°. 32 frequencies were acquired at offsets: ± 10 (twice), ± 5.0 , ± 2.5 , ± 2.0 , ± 1.5 , ± 1.2 , ± 1.0 , ± 0.80 , ± 0.70 , ± 0.60 , ± 0.50 , ± 0.40 , ± 0.30 , ± 0.20 , ± 0.10 ppm. The total time per frequency point was 1200 ms and one full Z-spectrum took 38.4 s to acquire. In total 40 dynamics (Z-spectra) were acquired. Approximately five minutes into the scan, D-Glc was administered intravenously at a rate of 6.25 g/min using hospital-grade D50 glucose (D50, Hospira, Inc., Lake Forest, IL; 35 g of D-Glc in 70 mL of water sterile solution prepared by the Johns Hopkins pharmacy), followed by a saline rinse. Total experiment duration was 25.5 min.

A T_1 -weighted gradient-echo sequence was used for DCE MRI: TR/TE/FA=5.1 ms/2.5 ms/26°, FOV=212×212 mm², resolution=2.2×2.2×4.4 mm³. Gadoteridol (ProHance, Bracco Diagnostics) was given at a dosage of 0.1 mmol/kg via a power injector. The contrast agent was injected with an injection delay of 30 seconds (15 pre-contrast baseline images) at a speed of 5 mL/s, followed by a saline rinse. Each 15-slice dynamic scan was 2.0 s, and a total of 150 dynamics were acquired. A post-contrast MPRAGE image was acquired after the DCE series.

Approximately 7 min after the first Gd contrast injection, a second dose of Gd was injected for performing DSC imaging. DSC images were acquired using single-shot EPI with TR/TE/FA=1344 ms/29 ms/90°, FOV=212×212 mm², and resolution=2.2×2.2×4.4 mm³. The contrast agent was injected with a 15-second injection delay (11 pre-contrast baseline images) at a speed of 5 mL/s, followed by a saline rinse. A total of 100 dynamics were acquired for 25 slices covering most of the brain.

2.3 Post-Processing

2.3.1 DS-DGE MRI

The dynamic DS spectrum in each voxel was fitted to a Lorentzian line shape using the single Lorentzian fitting neural network (sLoFNet), a DL-based approach that has shown robustness and improved time efficiency [43]. The linewidths, defined as full width at half maximum height (FWHM) in the DL fitting, were used to generate LW maps (in Hz) for each dynamic. Retrospective rigid motion correction using Elastix [49] was applied to the dynamic linewidth maps and visually inspected for remaining motion artefacts.

To obtain dynamic ΔLW images and normalized area-under-the-curve (AUC) maps, a baseline was calculated by averaging the linewidth maps obtained before infusion. To remove outliers, baseline signals that were greater or less than the average $\pm 2\text{SD}$ were discarded, and LW_{base} was calculated using the remaining baseline signals. ΔLW images were obtained by subtracting LW_{base} from each linewidth dynamic image, $LW(t)$, followed by normalization with LW_{base} . Normalized AUC was calculated by subtracting LW_{base} from the averaged dynamic linewidth maps (obtained during infusion and post-infusion) LW_{average} , followed by normalization with LW_{base} :

$$\Delta\text{LW}(t)(\%) = \frac{LW(t) - LW_{\text{base}}}{LW_{\text{base}}} \times 100\% \quad (2)$$

$$\text{AUC}(\%) = \frac{LW_{\text{average}} - LW_{\text{base}}}{LW_{\text{base}}} \times 100\% \quad (3)$$

Both the fitting and the calculations were performed in Python.

2.3.2 DCE and DSC MRI

The dynamic images obtained from DCE and DSC MRI were processed using the software OLEA Sphere (Olea Medical Solutions, La Ciotat, France). For both sequences, the dynamic images were motion-corrected before the perfusion and perfusion-related parameters were calculated. The extended Toft Model was used for DCE-MRI [50] to retrieve maps of the interstitial volume (V_e) and the volume transfer constant (K^{trans}), which represents a combination of permeability and perfusion. For the DSC-MRI, standard tracer kinetic modeling, together with a leakage correction algorithm, was applied to

obtain leakage corrected cerebral blood volume (corr. CBV), uncorrected cerebral blood volume (uncorr. CBV) and leakage (K2) [51, 52].

3 Results

Figure 1 shows the simulated Z-spectra for the different tissues with and without glucose infusion. The simulated baseline LWs were 87 Hz for blood, 57 Hz for arterial blood, 96 Hz for venous blood, 65 Hz for GM, 60 Hz for WM, 42 Hz for TUMOR, and 16 Hz for CSF. The simulated linewidth difference ΔLW was 0.56% for blood, 1.3% for arterial blood, 0.30% for venous blood, 0.29% for GM, 0.34% for WM, 7.5% for TUMOR, and 13% for CSF.

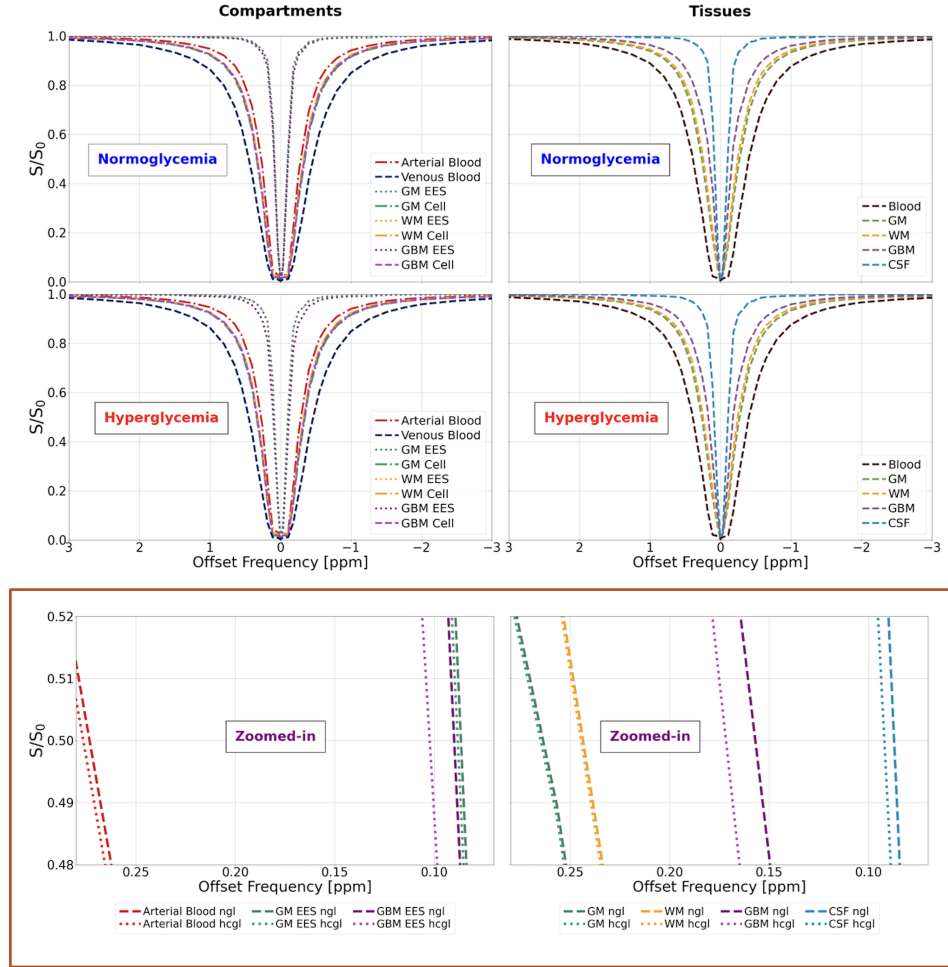


Figure 1: Normoglycemic ($C_p^a = 6.15$ mM) and hyperglycemic ($C_p^a = 19.8$ mM) simulated Z-spectra for tissue compartments (left) and total tissue (right). The lower row shows a zoomed-in view comparing the Z-spectral intensities around half-maximum for normo- and hyperglycemia. Only Z-spectra with a sufficiently large change are visualized for tissue compartments (lower left). Saturation parameters: $B_{1\text{peak}}$ of $0.5 \mu\text{T}$, ten consecutive 50-ms sinc-gauss pulses for $t_{\text{sat}} = 0.5\text{s}$, $\text{TR} = 1.2\text{s}$).

Figure 2 shows a patient with a recurrent IDH-wildtype glioblastoma with thin peripheral contrast-enhancement (Gd- T_1w) around the resection cavity and surrounding expansile infiltrative FLAIR hyperintense tumor. Dynamic ΔLW images obtained upon infusing D-Glc are shown (averaged over two dynamics). Note the LW increase in vascular, CSF and tumor tissue. For DCE, K^{trans} shows an increase in the same regions while V_e shows only a slight increase. Both K^{trans} and V_e are hypointense in the cavity. The DS-DGE AUC map also displays an increase in the surrounding tumor and a hypointense core. For DSC, K2 shows enhancement comparable to DS-DGE. During the D-Glc infusion, the DS-DGE linewidth increased approximately to 15% for the contrast enhanced peri-cavity infiltrative tumor region and 40% for ventricular CSF.

Figure 3 shows experimental Z-spectra before and after D-Glc infusion together with DL Lorentzian fits for region-of-interests (ROIs) in the anterior cerebral artery, GM, WM, tumor tissue, and CSF (ventricle). Notice that the linewidths, as well as

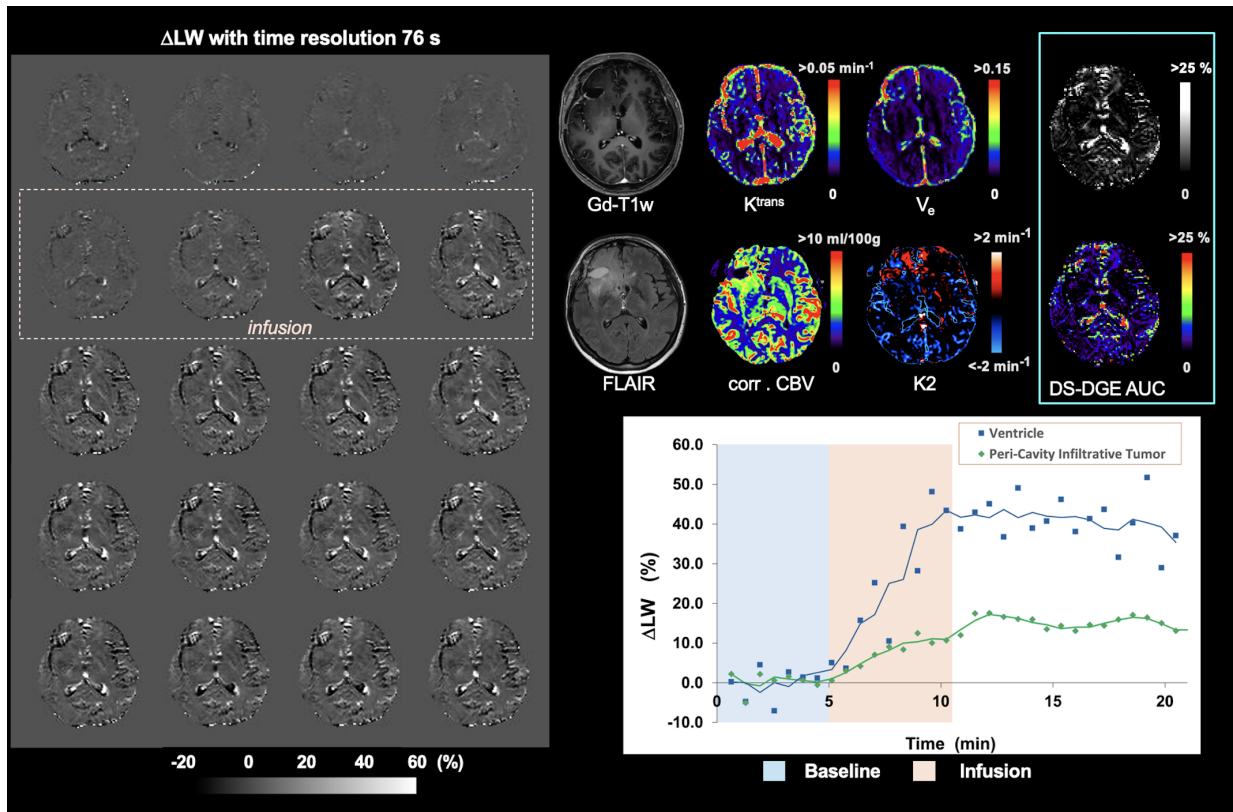


Figure 2: Images for a patient with a recurrent IDH-wildtype glioblastoma showing thin Gd-enhancement around the resection cavity. (Left) ΔLW maps during the scan (averaged over a period 76 s corresponding to two ΔLW images). (Right top) Anatomical images (Gd- T_{1w} , FLAIR), together with parametric maps from DCE MRI (K^{trans} , V_e), DSC MRI (corrected CBV, K_2) and DS-DGE MRI (AUC grayscale and color-coded). (Right bottom) Graphs of linewidth change vs time obtained from ROIs placed in the DS-DGE peri-cavity infiltrative tumor region, located anterior to the cavity, and ventricle (blue squares and green diamonds). To visualize the trend of the glucose uptake, $\Delta LW(t)$ curves were temporally smoothed with a 3-point moving average (blue and green lines).

their broadening, are similar to the simulated data in Figure 1. However, the *in vivo* changes in arterial blood and CSF were generally larger than those in the simulations.

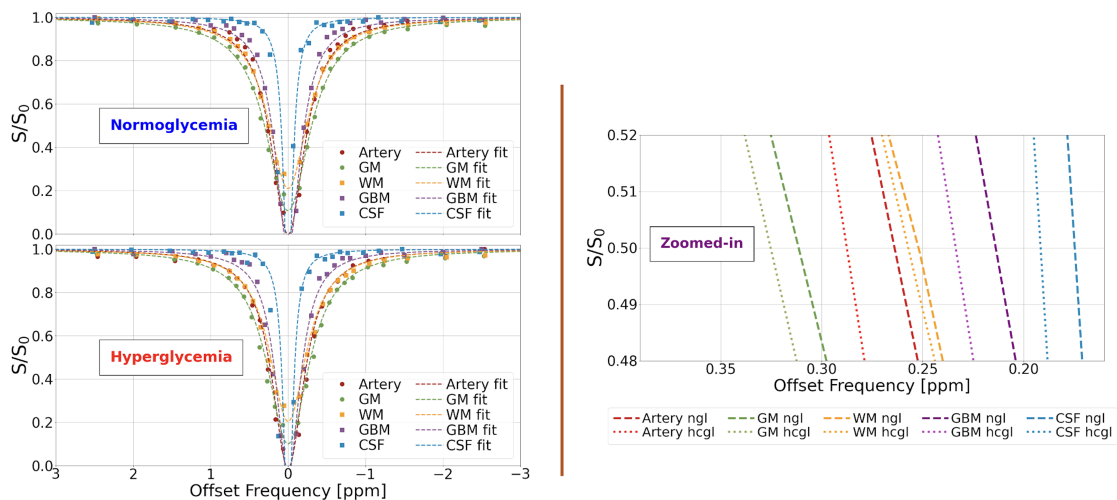


Figure 3: (Left) Normoglycemic (ngl) and hyperglycemic (hagl) experimental Z-spectra from the glioblastoma patient in Fig. 2 and the corresponding DL Lorentzian fits. (Right) A zoomed-in view demonstrating the linewidth difference between normo- and hyperglycemic experimental Z-spectra.

Figure 4 shows a patient with a grade 2 IDH-mutated astrocytoma. Interestingly, the enhanced tumor rim in the DS-DGE AUC image corresponds approximately to the spatial difference between the hypointense area in Gd-T₁w and the hyperintense area in FLAIR. Corrected CBV and K₂ also show some increase in the corresponding area. However, K^{trans} and V_e appear normal.

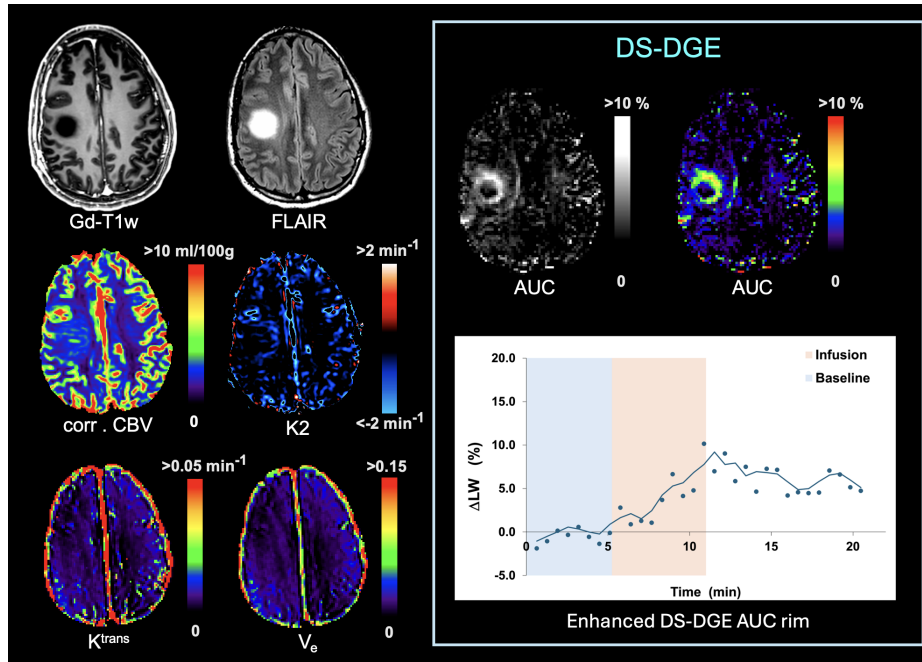


Figure 4: Patient with grade 2 IDH-mutated Astrocytoma. Anatomical images (Gd-T₁w, FLAIR) together with parametric maps from DSC MRI (corrected CBV, K₂), DCE MRI (K^{trans}, V_e), and DS-DGE MRI (AUC in both grayscale and color-coded). Graphs of linewidth change vs time obtained from ROI placed in the DS-DGE contrast-enhanced area (blue dots). To visualize the trend of the glucose uptake, ΔLW(t) curves were temporally smoothed with a 3-point moving average (blue line).

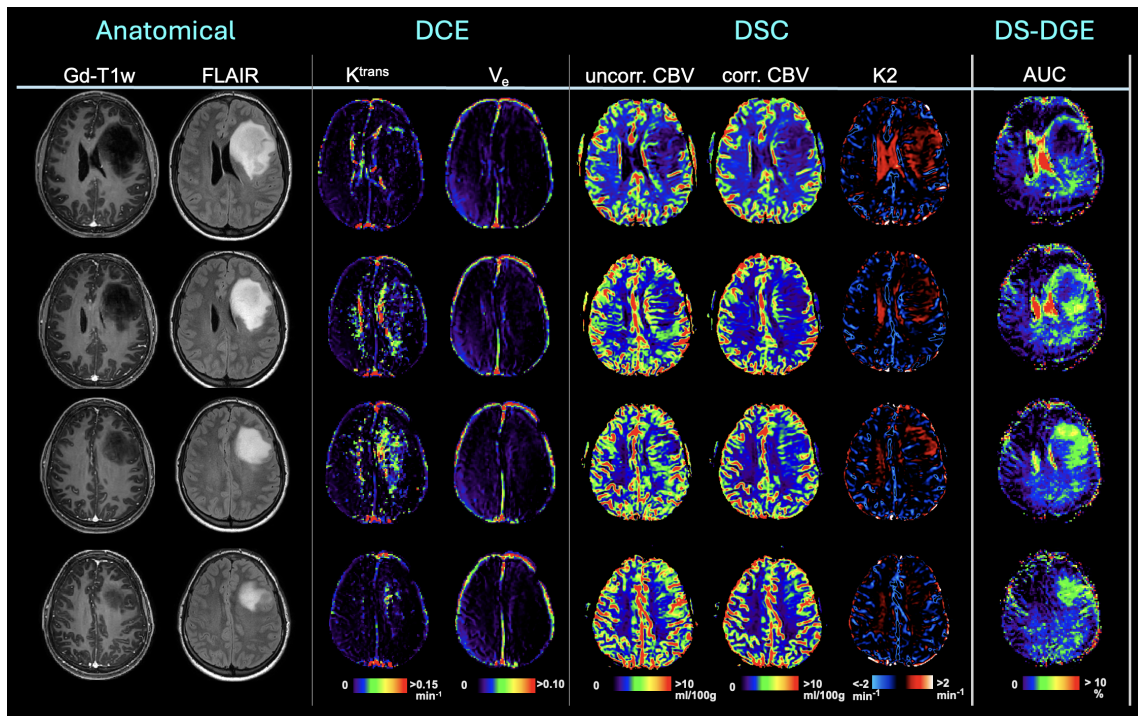


Figure 5: Patient with a grade 2 IDH-mutated astrocytoma. Anatomical images (Gd-T₁w, FLAIR) together with parametric maps from DCE MRI (K^{trans}, V_e), DSC MRI (uncorrected CBV, corrected CBV, K₂) and DS-DGE MRI (color-coded) from four slices.

Figure 5 shows four slices from a patient with a grade 2 IDH-mutated astrocytoma. K^{trans} shows an increase in the tumor boundary, while V_e shows only a slight increase. Similar to the patient in Figure 1, the lesion area visible in the uncorrected CBV is strongly reduced, both in intensity and area, after leakage correction, as reflected well in the K2 enhancement. Note that DS-DGE hyperintense and hypointense tumor regions correspond approximately to the hyperintense rim and hypointense core in the FLAIR image, respectively. The K2 images show a similar trend but over a smaller region.

Figure 6 shows results for a patient with ALK-mutated non-small-cell lung cancer brain metastases. K^{trans} and V_e are increased in the Gd-contrast-enhanced lesion area. The DS-DGE ΔLW time curve shows a continuous increase up to approximately 20% in the DS-DGE contrast-enhanced lesion. The DS-DGE AUC map also displays an increase in part of the lesion area, whereas the white matter shows negligible LW change. Note that the high values in the lesion area in the uncorrected CBV are strongly reduced after leakage correction. The enhancement observed on the contralateral side in the DS-DGE map is due to ventricular CSF.

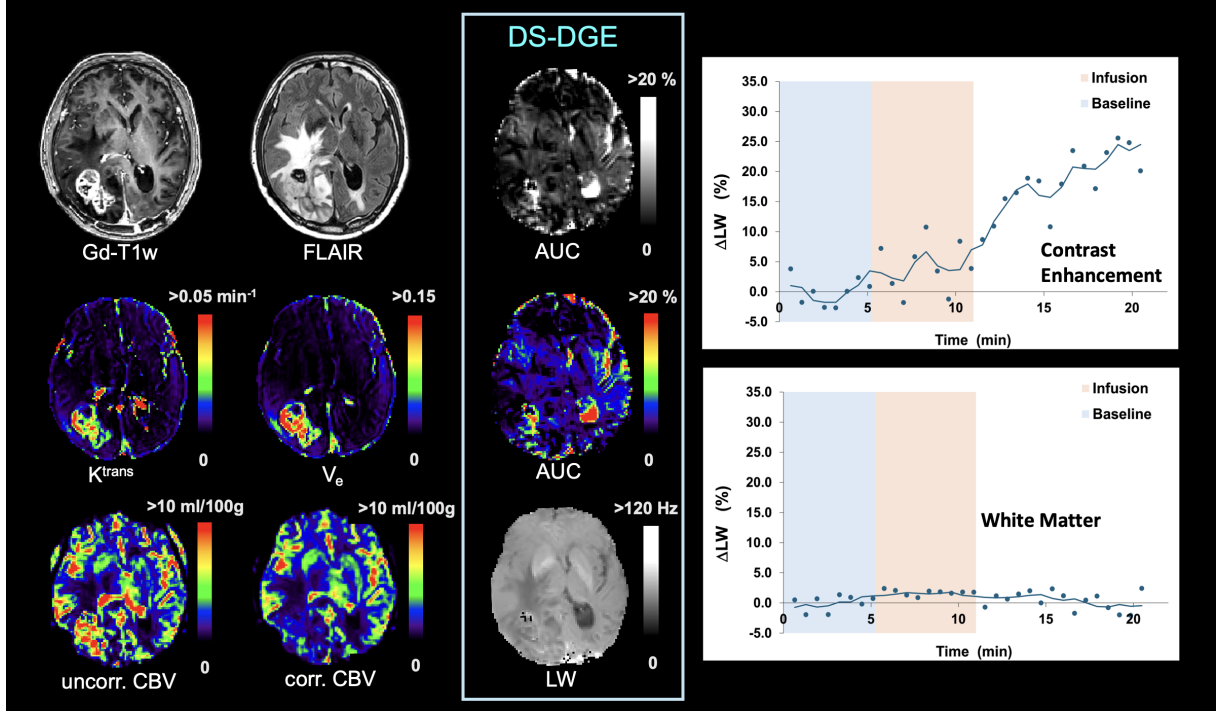


Figure 6: Patient with brain metastasis from ALK-mutated non-small-cell lung cancer. Anatomical images (Gd-T1w, FLAIR) together with parametric maps from DCE MRI (K^{trans} , V_e), DSC MRI (uncorrected CBV, corrected CBV) and DS-DGE MRI (LW map from 3rd dynamic, AUC maps in both grayscale and color-coded). Graphs of linewidth change vs. time obtained from ROIs placed in the DS-DGE contrast-enhanced area and contralateral frontal WM are shown to the right (blue dots). To visualize the trend of the glucose uptake, $\Delta\text{LW}(t)$ curves were temporally smoothed with a 3-point moving average (blue lines).

4 Discussion

We developed and implemented DS-DGE MRI to dynamically assess D-Glc uptake in brain tumors. This approach samples Z-spectra dynamically, which has the advantages of (i) multiple signal points per dynamic (leading to higher SNR and reduced sensitivity to motion due to the Lorentzian fitting), (ii) being independent of B_0 changes in the voxel between dynamics, e.g. such as those due to motion, as the full DS spectrum is fitted and (iii) a water resonance line shape that has minimal contributions from CEST, rNOE and MTC effects and can be approximated by a Lorentzian curve [40, 42, 53-55]. When applying RF saturation with low B_1 , the width at half-height of the DS Z-spectral line can be calculated as:

$$LW = FWHM = \left(\frac{1}{\pi}\right) \sqrt{\frac{R_1 R_2^2 + \omega_1^2 R_2}{R_1}} \approx \left(\frac{1}{\pi}\right) \sqrt{\frac{\omega_1^2 R_2}{R_1}}, \quad (4)$$

in which $\omega_1 = \gamma B_1$ (in units of rad/s) and $R_{1,2} = 1/T_{1,2}$. The presence of exchangeable protons at an offset from the water resonance will increase R_2 [38, 39] and broaden this line shape, with relative effects expected to be largest for the compartments

with a long water T_2 . This was borne out in the simulations, where EES and CSF exhibited narrow lines and large linewidth changes when the D-Glc concentration was increased (Fig. 1). When compartments were added proportionally (Eq. 1) to generate the Z-spectra for different tissues, ΔLW was highest in TUMOR which can be attributed to (i) the large concentration of D-Glc in EES after BBB breakdown, (ii) increased blood volume and EES volume, and (iii) the lower pH in the EES, which reduces the exchange rate and increases the exchange-based transverse relaxivity. For blood, despite having the highest concentration of D-Glc, simulations showed a smaller change in linewidth, which we attribute to the shorter T_2 originating from the high protein contents in both plasma (albumin) and erythrocyte (hemoglobin). Notice that an equal water-based concentration of D-Glc in plasma and erythrocytes [56-58] was used, removing any effect of microvascular hematocrit on blood D-Glc concentrations. The small effects in WM and GM are attributed to the low concentration of D-Glc in EES and even lower in the cells due to facilitated transport over the BBB and the cell membrane, respectively, and metabolism in the cell. The short T_2 of the cell compartment, which occupies a large volume fraction of the tissue, further reduces the DS-DGE effect size.

In patients, the effect sizes for the DS-DGE linewidth differences, $\Delta LW(t)$, were generally on the same order of magnitude of those obtained from simulations. This can be observed in Fig. 6, where the WM uptake curve shows a small increase during and after D-Glc infusion, and GM and WM intensities in the AUC maps are close to zero. The same is true for the DS-DGE AUC maps in Figs. 2, 4, and 5. CSF had a smaller ΔLW in the simulations than sometimes observed in the experimental data (approx. 15% compared to up to 40%, Figure 2). This difference may be due to the deviation from a Lorentzian line shape due to so-called sidebands appearing as distinct patterns when using short RF pulses at high sampling rates [59]. Sidebands are prone to occur in tissues with relatively long T_2 such as CSF or other liquid environments as necrotic tumor tissue [59]. Interestingly, the maximum LW increases in blood and CSF (Fig. 2) *in vivo* were found to be larger than those from the simulations (Fig. 1). One potential explanation for blood could be an osmotic increase in water content of blood due to the higher D-Glc concentration and a concomitant increase in T_2 , previously suggested as a potential contributor to signal changes in CESL [26, 60]. Another potential explanation is that the increase in plasma blood glucose concentration, and subsequently the CSF, may be greater than what we assumed in our simulations. Previous DGE studies have reported increases up to 15 mM in plasma blood glucose [13, 30] for a maximum D-Glc dose of 25 g, while our study used 35 g. If this increase proves to be reproducible in blood, it could allow the retrieval of an arterial input function for deconvolving the tumor tissue curve, resulting in a dynamic time curve that could provide information about glucose transport and metabolism. However, this is beyond the goal of this technical feasibility study.

The experimental data showed that several tumor tissues had a larger LW increase than GM and WM (Figs. 2-6), confirming the simulations. In all four tumor cases, BBB leakage in the tumor was visible in K2 images or when comparing uncorrected CBV with corrected CBV in areas coinciding spatially with part of the DS-DGE enhancement. However, the DS-DGE enhancement area was generally larger and more pronounced in intensity. K^{trans} and V_e , to some degree, also showed overlap with DS-DGE enhancements. Additional patient studies are needed to draw more substantial conclusions, but these first results are highly encouraging showing the feasibility for DS-DGE to outline tumor tissue with BBB disruption even before Gd-enhancement can detect it. Another important aspect is that the large effect in malignant tumor, combined with a small effect in normal tissue, constitutes an advantage over PET studies of brain malignancies, where phosphorylated ^{19}F -deoxyglucose signal builds up in both brain tumors and healthy gray matter.

There are several practical considerations that need to be mentioned. First, similar to other DGE studies, our scan time was long, which increases the risk of motion, which may introduce tissue mixing, resulting in hypo- and hyperintensities in the (DS)-DGE maps [36, 37]. In addition, motion can shift the voxel to another position, resulting in erroneous $\Delta LW(t)$ curves. As motion correction can reduce these errors [35], we applied this to our dynamic data. However, care must be taken so that true effects are not also removed or reduced by interpolation errors. Furthermore, while motion correction was applied to the dynamic LW images, the individual frequency offset images were not corrected for motion, however these can also be affected by motion. Such a frequency-specific motion correction can be more challenging due to the intensity differences between the offsets in the dynamic Z-spectrum. On the other hand, the Lorentzian fitting over a large number of points is performed using a pre-determined line shape, which may reduce small motion effects on the measured LW. Second, this study used a D-Glc dose of 35 g (0.5 g/kg up to a maximum of 35 g), while previous studies have used a maximum dose of 25 g, leading to smaller effects. For example, the first DGE MRI study at 3 T by Xu et al. gave an effect size of approximately 1.5% in glioblastoma [32]. In a larger patient cohort, Mo et al. found effect sizes of 0.5-1.5% in low (LGG) and high grade glioma (HGG) enhancement areas using a dose of 25 g [61]. A smaller maximum dose (20 g of D-Glc in 100 mL) was used by Bender et al. in LGG and HGG patients resulting in effect sizes of maximum 0.25% in the contrast enhanced tumor area [29]. For metastases, a recent DGE MRI study by Wu et al. [35] found up to a 10% increase after D-Glc infusion, while in our study, the metastases showed an increase of more than 20%. However, it is difficult to make a quantitative comparison between these

studies since they differ in saturation parameters, D-Glc concentration, and contrast origin, i.e., CEST including T_2 relaxation versus linewidth change based on T_2 relaxation. In addition, these differences can be caused by individual variations of the tumor structure and properties, warranting a larger population study. Third, since we are acquiring the Z-spectra during a steady state, an additional signal decrease will occur as a function of time during the acquisition of the Z-spectrum. Although the frequency offsets are acquired in alternating fashion around the water frequency, this continuous signal decrease will still cause the DS to deviate from a true Lorentzian line shape. This may especially affect the narrower line shapes where fitting deviations may occur at the earlier smaller intensity drops in the Z-spectrum (Figs. 1 and 3).

5 Conclusions

We developed DS-DGE MRI to assess D-Glc uptake in brain tumors. Contrary to glucoCESL- and single-frequency glucoCEST-based DGE MRI, this approach is inherently independent of B_0 shifts occurring between the dynamics. Whole-brain dynamic Z-spectral images were acquired in less than 40 seconds, allowing imaging of D-Glc uptake curves in multiple tissues. Early patient data look highly promising, with DS-DGE highlighting lesion areas with similar and/or complementary information to Gd-based PWI. DS-DGE MRI can thus further bridge the gap between research and clinical implementation of using D-Glc as a biodegradable contrast agent.

6 Acknowledgments

We are grateful to Terri Brawner, Kathleen Kahl, Ivana Kusevic, and Maia Lee for their assistance with the experiments. Under a license agreement between Philips and the Johns Hopkins University, Dr. Knutsson's spouse, Dr. van Zijl, and the University are entitled to fees related to an imaging device used in the study discussed in this publication. Dr. van Zijl is also a paid lecturer for Philips. This arrangement has been reviewed and approved by the Johns Hopkins University in accordance with its conflict of interest policies. This project was supported by National Institutes of Health grant number RO1 EB034978; Swedish Research Council grant number 2019-03637; Swedish Cancer Society grant number 21 1652 Pj;

7 Data availability statement

The data that support the findings of this study are available from the corresponding author upon reasonable request.

8 References

1. Mathur M, Jones JR, Weinreb JC. Gadolinium Deposition and Nephrogenic Systemic Fibrosis: A Radiologist's Primer. *Radiographics*. 2020;40(1):153-62.
2. Woolen SA, Shankar PR, Gagnier JJ, MacEachern MP, Singer L, Davenport MS. Risk of Nephrogenic Systemic Fibrosis in Patients With Stage 4 or 5 Chronic Kidney Disease Receiving a Group II Gadolinium-Based Contrast Agent: A Systematic Review and Meta-analysis. *JAMA Intern Med*. 2020;180(2):223-30.
3. Gulani V, Calamante F, Shellock FG, Kanal E, Reeder SB, International Society for Magnetic Resonance in M. Gadolinium deposition in the brain: summary of evidence and recommendations. *Lancet Neurol*. 2017;16(7):564-70.
4. McDonald RJ, McDonald JS, Kallmes DF, Jentoft ME, Paolini MA, Murray DL, et al. Gadolinium Deposition in Human Brain Tissues after Contrast-enhanced MR Imaging in Adult Patients without Intracranial Abnormalities. *Radiology*. 2017;285(2):546-54.
5. Lord ML, Chettle DR, Grafe JL, Noseworthy MD, McNeill FE. Observed Deposition of Gadolinium in Bone Using a New Noninvasive in Vivo Biomedical Device: Results of a Small Pilot Feasibility Study. *Radiology*. 2018;287(1):96-103.
6. U.S. Food and Drug Administration. (2017). FDA-approved labeling for healthcare professionals: Boxed warning section. FDA document no. 105513. Retrieved from: www.fda.gov/media/105513/download. Date Accessed: September 23, 2024.
7. Eichberg DG, Di L, Morell AA, Shah AH, Semonche AM, Chin CN, et al. Incidence of high grade gliomas presenting as radiographically non-enhancing lesions: experience in 111 surgically treated non-enhancing gliomas with tissue diagnosis. *J Neurooncol*. 2020;147(3):671-9.
8. Marta GN, da Cunha Colombo Bonadio RR, Martins RE, Zuppani HB, de Castro GJ. Cystic brain metastases in ALK-rearranged non-small cell lung cancer. *Ecancermedicalscience*. 2018;12:818.
9. Falk Delgado A, Van Westen D, Nilsson M, Knutsson L, Sundgren PC, Larsson EM, et al. Diagnostic value of alternative techniques to gadolinium-based contrast agents in MR neuroimaging-a comprehensive overview. *Insights Imaging*. 2019;10(1):84.
10. Ward KM, Aletras AH, Balaban RS. A new class of contrast agents for MRI based on proton chemical exchange dependent saturation transfer (CEST). *J Magn Reson*. 2000;143(1):79-87.
11. Chan KW, McMahon MT, Kato Y, Liu G, Bulte JW, Bhujwala ZM, et al. Natural D-glucose as a biodegradable MRI contrast agent for detecting cancer. *Magn Reson Med*. 2012;68(6):1764-73.
12. Walker-Samuel S, Ramasawmy R, Torrealdea F, Rega M, Rajkumar V, Johnson SP, et al. In vivo imaging of glucose uptake and metabolism in tumors. *Nat Med*. 2013;19(8):1067-72.
13. Xu X, Yadav NN, Knutsson L, Hua J, Kalyani R, Hall E, et al. Dynamic glucose-enhanced (DGE) MRI: translation to human scanning and first results in glioma patients. *Tomography*. 2015;1(2):105-14.
14. Xu X, Chan KW, Knutsson L, Artemov D, Xu J, Liu G, et al. Dynamic glucose enhanced (DGE) MRI for combined imaging of blood-brain barrier break down and increased blood volume in brain cancer. *Magn Reson Med*. 2015;74(6):1556-63.
15. Rivlin M, Navon G. Glucosamine and N-acetyl glucosamine as new CEST MRI agents for molecular imaging of tumors. *Sci Rep*. 2016;6:32648.
16. Knutsson L, Xu J, Ahlgren A, van Zijl PCM. CEST, ASL, and magnetization transfer contrast: How similar pulse sequences detect different phenomena. *Magn Reson Med*. 2018;80(4):1320-40.
17. Knutsson L, Xu X, van Zijl PCM, Chan K W Y. Imaging of sugar-based contrast agents using their hydroxyl proton exchange properties. *NMR Biomed*. 2022:e4784.
18. Jin T, Autio J, Obata T, Kim SG. Spin-locking versus chemical exchange saturation transfer MRI for investigating chemical exchange process between water and labile metabolite protons. *Magn Reson Med*. 2011;65(5):1448-60.
19. Cobb JG, Xie J, Li K, Gochberg DF, Gore JC. Exchange-mediated contrast agents for spin-lock imaging. *Magn Reson Med*. 2012;67(5):1427-33.
20. Yuan J, Zhou J, Ahuja AT, Wang YX. MR chemical exchange imaging with spin-lock technique (CESL): a theoretical analysis of the Z-spectrum using a two-pool R(1rho) relaxation model beyond the fast-exchange limit. *Phys Med Biol*. 2012;57(24):8185-200.
21. Zaiss M, Bachert P. Exchange-dependent relaxation in the rotating frame for slow and intermediate exchange -- modeling off-resonant spin-lock and chemical exchange saturation transfer. *NMR Biomed*. 2013;26(5):507-18.

22. Jin T, Mehrens H, Hendrich KS, Kim SG. Mapping brain glucose uptake with chemical exchange-sensitive spin-lock magnetic resonance imaging. *J Cereb Blood Flow Metab.* 2014;34(8):1402-10.
23. Schuenke P, Paech D, Koehler C, Windschuh J, Bachert P, Ladd ME, et al. Fast and quantitative T1rho-weighted dynamic glucose enhanced MRI. *Sci Rep.* 2017;7:42093.
24. Schuenke P, Koehler C, Korzowski A, Windschuh J, Bachert P, Ladd ME, et al. Adiabatically prepared spin-lock approach for T1rho-based dynamic glucose enhanced MRI at ultrahigh fields. *Magn Reson Med.* 2017;78(1):215-25.
25. Paech D, Schuenke P, Koehler C, Windschuh J, Mundiyanapurath S, Bickelhaupt S, et al. T1rho-weighted dynamic glucose-enhanced MR imaging in the human brain. *Radiology.* 2017;285(3):914-22.
26. Jin T, Iordanova B, Hitchens TK, Modo M, Wang P, Mehrens H, et al. Chemical exchange-sensitive spin-lock (CESL) MRI of glucose and analogs in brain tumors. *Magn Reson Med.* 2018;80(2):488-95.
27. Herz K, Lindig T, Deshmane A, Schittenhelm J, Skardelly M, Bender B, et al. T1rho-based dynamic glucose-enhanced (DGERho) MRI at 3 T: method development and early clinical experience in the human brain. *Magn Reson Med.* 2019;82(5):1832-47.
28. Boyd PS, Breitling J, Zimmermann F, Korzowski A, Zaiss M, Schuenke P, et al. Dynamic glucose-enhanced (DGE) MRI in the human brain at 7 T with reduced motion-induced artifacts based on quantitative R1rho mapping. *Magn Reson Med.* 2020;84(1):182-91.
29. Bender B, Herz K, Deshmane A, Richter V, Tabatabai G, Schittenhelm J, et al. GLINT: GlucoCEST in neoplastic tumors at 3 T-clinical results of GlucoCEST in gliomas. *MAGMA.* 2022;35(1):77-85.
30. Knutsson L, Seidemo A, Rydhog Scherman A, Markenroth Bloch K, Kalyani RR, Andersen M, et al. Arterial Input Functions and Tissue Response Curves in Dynamic Glucose-Enhanced (DGE) Imaging: Comparison Between glucoCEST and Blood Glucose Sampling in Humans. *Tomography.* 2018;4(4):164-71.
31. Xu X, Xu J, Knutsson L, Liu J, Liu H, Li Y, et al. The effect of the mTOR inhibitor rapamycin on glucoCEST signal in a preclinical model of glioblastoma. *Magn Reson Med.* 2019;81(6):3798-807.
32. Xu X, Sehgal AA, Yadav NN, Larterra J, Blair L, Blakeley J, et al. D-glucose weighted chemical exchange saturation transfer (glucoCEST)-based dynamic glucose enhanced (DGE) MRI at 3T: early experience in healthy volunteers and brain tumor patients. *Magn Reson Med.* 2020;84(1):247-62.
33. Seidemo A, Lehmann PM, Rydhog A, Wirestam R, Helms G, Zhang Y, et al. Towards robust glucose chemical exchange saturation transfer imaging in humans at 3 T: Arterial input function measurements and the effects of infusion time. *NMR Biomed.* 2022;35(2):e4624.
34. Seidemo A, Wirestam R, Helms G, Markenroth Bloch K, Xu X, Bengzon J, et al. Tissue response curve-shape analysis of dynamic glucose-enhanced and dynamic contrast-enhanced magnetic resonance imaging in patients with brain tumor. *NMR Biomed.* 2023;36(6):e4863.
35. Wu Y, Derks S, Wood TC, de Blois E, van der Veldt AAM, Smits M, et al. Improved postprocessing of dynamic glucose-enhanced CEST MRI for imaging brain metastases at 3 T. *Eur Radiol Exp.* 2023;7(1):78.
36. Zaiss M, Herz K, Deshmane A, Kim M, Golay X, Lindig T, et al. Possible artifacts in dynamic CEST MRI due to motion and field alterations. *J Magn Reson.* 2019;298:16-22.
37. Lehmann PM, Seidemo A, Andersen M, Xu X, Li X, Yadav NN, et al. A numerical human brain phantom for dynamic glucose-enhanced (DGE) MRI: On the influence of head motion at 3T. *Magn Reson Med.* 2023;89(5):1871-87.
38. Gore JC, Brown MS, Mizumoto CT, Armitage IM. Influence of glycogen on water proton relaxation times. *Magn Reson Med.* 1986;3(3):463-6.
39. Yadav NN, Xu J, Bar-Shir A, Qin Q, Chan KW, Grgac K, et al. Natural D-glucose as a biodegradable MRI relaxation agent. *Magn Reson Med.* 2014;72(3):823-8.
40. Kim M, Gillen J, Landman BA, Zhou J, van Zijl PC. Water saturation shift referencing (WASSR) for chemical exchange saturation transfer (CEST) experiments. *Magn Reson Med.* 2009;61(6):1441-50.
41. Zhou Y, Bie C, van Zijl PCM, Yadav NN. The relayed nuclear Overhauser effect in magnetization transfer and chemical exchange saturation transfer MRI. *NMR Biomed.* 2023;36(6):e4778.
42. Liu G, Qin Q, Chan KW, Li Y, Bulte JW, McMahon MT, et al. Non-invasive temperature mapping using temperature-responsive water saturation shift referencing (T-WASSR) MRI. *NMR Biomed.* 2014;27(3):320-31.
43. Mohammed Ali S, Yadav NN, Wirestam R, Singh M, Heo HY, van Zijl PC, et al. Deep learning-based Lorentzian fitting of water saturation shift referencing spectra in MRI. *Magn Reson Med.* 2023;90(4):1610-24.

44. Herz K, Mueller S, Perlman O, Zaitsev M, Knutsson L, Sun PZ, et al. Pulseseq-CEST: Towards multi-site multi-vendor compatibility and reproducibility of CEST experiments using an open-source sequence standard. *Magn Reson Med*. 2021;86(4):1845-58.
45. Seidemo A, Knutsson L, Yadav NN, Sundgren PC, Wirestam R, van Zijl PCM. A three-tissue-compartment model for cerebral glucose delivery, transport and metabolism: Theory and modeling. 2024.
46. Shestov AA, Emir UE, Kumar A, Henry PG, Seaquist ER, Oz G. Simultaneous measurement of glucose transport and utilization in the human brain. *Am J Physiol Endocrinol Metab*. 2011;301(5):E1040-9.
47. Zaiss M, Anemone A, Goerke S, Longo DL, Herz K, Pohmann R, et al. Quantification of hydroxyl exchange of D-Glucose at physiological conditions for optimization of glucoCEST MRI at 3, 7 and 9.4 Tesla. *NMR Biomed*. 2019;32(9):e4113.
48. Lu H, Golay X, Pekar JJ, Van Zijl PC. Sustained poststimulus elevation in cerebral oxygen utilization after vascular recovery. *J Cereb Blood Flow Metab*. 2004;24(7):764-70.
49. Klein S, Staring M, Murphy K, Viergever MA, Pluim JP. elastix: a toolbox for intensity-based medical image registration. *IEEE Trans Med Imaging*. 2010;29(1):196-205.
50. Tofts PS. Modeling tracer kinetics in dynamic Gd-DTPA MR imaging. *J Magn Reson Imaging*. 1997;7(1):91-101.
51. Knutsson L, Stahlberg F, Wirestam R. Absolute quantification of perfusion using dynamic susceptibility contrast MRI: pitfalls and possibilities. *MAGMA*. 2010;23(1):1-21.
52. Knutsson L, Lindgren E, Ahlgren A, van Osch MJ, Bloch KM, Surova Y, et al. Dynamic susceptibility contrast MRI with a prebolus contrast agent administration design for improved absolute quantification of perfusion. *Magn Reson Med*. 2014;72(4):996-1006.
53. Mulkern RV, Williams ML. The general solution to the Bloch equation with constant rf and relaxation terms: application to saturation and slice selection. *Med Phys*. 1993;20(1):5-13.
54. Smith SA, Bulte JW, van Zijl PC. Direct saturation MRI: theory and application to imaging brain iron. *Magn Reson Med*. 2009;62(2):384-93.
55. Lim IA, Li X, Jones CK, Farrell JA, Vikram DS, van Zijl PC. Quantitative magnetic susceptibility mapping without phase unwrapping using WASSR. *Neuroimage*. 2014;86:265-79.
56. Neely RD, Kiwanuka JB, Hadden DR. Influence of sample type on the interpretation of the oral glucose tolerance test for gestational diabetes mellitus. *Diabet Med*. 1991;8(2):129-34.
57. Farrer M, Albers CJ, Neil HA, Adams PC, Laker MF, Alberti KG. Assessing the impact of blood sample type on the estimated prevalence of impaired glucose tolerance and diabetes mellitus in epidemiological surveys. *Diabet Med*. 1995;12(4):325-9.
58. Carstensen B, Lindstrom J, Sundvall J, Borch-Johnsen K, Tuomilehto J, Group DPSS. Measurement of blood glucose: comparison between different types of specimens. *Ann Clin Biochem*. 2008;45(Pt 2):140-8.
59. Schure JR, Weinmuller S, Kamm L, Herz K, Zaiss M. Sidebands in CEST MR-How to recognize and avoid them. *Magn Reson Med*. 2024;91(6):2391-402.
60. Choi WM, Chung J, Jin T, Kim SG. Effect of osmolality on dynamic glucose enhanced (DGE) MRI. *25th Annual Meeting of ISMRM*; Honolulu, HI 2017. p. 194.
61. Mo J, Xu X, Ma A, Lu M, Wang X, Rui Q, et al. Dynamic glucose enhanced MRI of gliomas: a preliminary clinical application. *NMR Biomed*. 2024;In Press.
62. Li W, Grgac K, Huang A, Yadav N, Qin Q, van Zijl PC. Quantitative theory for the longitudinal relaxation time of blood water. *Magn Reson Med*. 2016;76(1):270-81.
63. Li W, van Zijl PCM. Quantitative theory for the transverse relaxation time of blood water. *NMR Biomed*. 2020;33(5):e4207. Erratum: Quantitative theory for the transverse relaxation time of blood water. *NMR Biomed*. 2020;33(8):e4329.